ADVANCED FUNCTIONAL MATERIALS
www.afm-journal.de

Elevating Biomedical Performance of ZnO/SiO_2@ Amorphous Calcium Phosphate - Bioinspiration Making Possible the Impossible

Duc-Viet Nguyen, Shengwei Jiang, Chengyong He, Zhongning Lin, Naibo Lin, Anh-Tuan Nguyen, Lifeng Kang, Ming-Yong Han, and Xiang-Yang Liu**

Here a biomimetic approach is presented to fabricate nanodragon fruits featured by a multitude of tiny quantum dot ZnO seeds embedded in mesosilica (SiO_2) flesh then enclosed in amorphous calcium phosphate (ACP) shell. The nanodragon fruits give rise to a new class of hybrid ZnO/SiO_2@ACP nanocomplex with multimoidal capability: cellular delivering, intracellular targeting, and subcellular imaging. With this particular design, the unusual fluorescent stability of ZnO quantum dots (QDs) in aqueous solution, the specific color selection of the functional ZnO QD seeds, and the stability of transient ACP over a long period of time are made possible. In addition, the nanodragon fruits, capable of targeting mitochondria, have elevated biocompatibility, thus can be of enormous potential applications in treating mitochondrial diseases including inflammation, neurodegeneration, obesity, diabetes, cardiovascular diseases, and cancer. As numerous human disorders are often associated with cellular dysfunctions, this biocompatible carrying platform, capable of delivering, targeting, and imaging subcellular organelles, is therefore highly desirable for efficacious therapeutic and diagnostic treatment.

1. Introduction

Numerous researches have indicated that in various functional materials, in particular soft materials, the macroscopic behavior begins to manifest itself not at the atomic or nanoscale but at the mesoscale.[1] It follows that the ability to predict and control mesoscale architectures is essential in tailor-making mesomaterials of specific functions.[2] After long evolution, some materials from living things, e.g., spider silk dragline fibers, butterfly wings, seashells, bones, etc. are of particular functions.[3–5] These functions are to a large extent subject to particular mesoscopic structures.[3–5] Thus we can acquire some specific functions by mimicking the mesostructures. In this paper, we will mimic the dragon fruit structure in the mesoscopic size in order to obtain enhanced biomedical performance of ZnO/SiO_2@ACP multiple core–shell nanospheres.

There is a growing interest in using nanocarriers for drug delivery, bioimaging, and biosensing as they offer high efficacious diagnostic and therapeutic treatment of human diseases. However, in order to reach the diseased cells and organelles, nanocarriers are often coupled with targeting moieties via ligand-exchange reactions, chemical or biological conjugation which are complicated and not always achievable. In the recent years, numerous nanoparticle systems (e.g., polymeric, noble metal, and semiconductor nanoparticles) have been

Dr. D.-V. Nguyen, Dr. A.-T. Nguyen, Prof. X.-Y. Liu
NUS Graduate School for Integrative Sciences and Engineering
Centre for Life Sciences (CeLS)
National University of Singapore
#05-01, 28 Medical Drive, Singapore 117456
E-mail: phyliuxy@nus.edu.sg
Dr. D.-V. Nguyen, Dr. A.-T. Nguyen, Prof. X.-Y. Liu
Department of Physics
National University of Singapore
Block S12, 2 Science Drive 3, Singapore 117551
S. W. Jiang, Dr. C. Y. He, Prof. Z. N. Lin
State Key Laboratory of Molecular Vaccinology and Molecular Diagnostics
School of Public Health
Xiamen University
Xiamen 361102, China
E-mail: linzhn@xmu.edu.cn
Dr. N. B. Lin, Prof. X.-Y Liu
Research Institute for Soft Matter and Biomimetics
Xiamen University
Fujian Provincial Key Laboratory for Soft Functional Materials Research and Fujian Provincial Key Laboratory of Fire Retardant Materials
Xiamen University
Xiamen 361102, P. R. China
Dr. L Kang
Department of Pharmacy
National University of Singapore
18 Science Drive 4, Singapore 117543
Dr. M.-Y. Han
Institute of Materials Research and Engineering
2 Fusionopolis Way, Singapore 138634

DOI: 10.1002/adfm.201601481

developed to target and deliver therapeutic/diagnostic payloads to mitochondria.[6] These nanosystems often involve the use of costly and toxic chemicals and need to follow complicated synthetic routes to further functionalize them with desired properties for these purposes. In addition, the applications of nanomaterials are also limited by their biocompatibility, biodegradation or physiochemical stability in biological environments. For examples, semiconductor nanocrystals (also known as QDs) are often synthesized in organic solvents, their fluorescence properties suffer from degradation when being transferred into aqueous solutions, and therefore they are normally required further functionalization prior to applications. The commonly used cadmium-based QDs have high toxicity with a fatal risk once cadmium is leaked from their carriers.[7,8] Another important material, carbon nanotubes are known to cause inflammatory response.[9] Furthermore, dendrimers, liposomes, or solid lipid nanoparticles are often found to be destabilized in biological environments due to the microbiological degradation.[10] Therefore, the strategies to overcome these downsides should be developed prior to their practical applications. One way to overcome the obstacle is to identify the new materials with high biocompatibility, suitable biostability, and controllable desired properties, which are not always achievable. The other way is to surpass the limitation by constructing a particular structure with controlled properties so that the desired performance can be produced. Due to the very rich selection, flexibility in both materials and engineering methods, this is always a highly desirable approach, compared with the first one.

To implement the second pathway, we adopt a bioinspired approach to mimic the structure of dragon fruits (pitahaya) in the mesoscale with enhanced biomedical performance. The fruit structure, with the simple yet so extraordinarily beautiful combination of shell, flesh, and seeds, provides a better way to protect functional seeds and acquire multifunctionalities for biomedical applications. If one can fabricate a biocompatible shell and flesh with a proper mesoscopic structure and desired properties, some extra benefits/functions such as the controlled release and targeted delivery of certain agents could be achieved. The well-controlled fabrication process can allow the precise selection of particular emission wavelengths, and the designated nanosized structure of dragon fruits will permit the long sustainable fluorescence emission of QDs in the aqueous environment and acquire the control release benefit. In this work, we demonstrate how to achieve the nanofruit structure, and show that the structure of nanosized dragon fruits, with suitable choice of materials, can deliver a better performance in terms of fluorescent stability and control, biocompatibility, targeting intracellular delivery, and subcellular imaging.

The hybrid ZnO/SiO_2@ACP nanostructures were designed and constructed according to the seed–flesh–shell structure of a nanosized fruits. The basic idea is that the shell provides the protection for the entire fruit while the flesh is the medium to stabilize and distribute the functional seeds. For biomedical applications, the shell requires the key consideration of biocompatibility, controlled release, and targeting delivery. For these reasons, calcium othorphosphate (CaP) based materials are excellent candidates for the shell construction as CaPs are ubiquitous in our body in the form of hard tissues (e.g., calcium hydroxyapatite in bone, teeth, etc.), thus they have unequivocal biocompatibility. In addition, they also have high bioactivity, biostability and bioavailability which are indispensable for biomedical applications.[11] The solubility of CaPs is pH dependent, and their morphologies, phases, polarization, surface properties are controlled by pH, supersaturation, additives, fields, etc.[12–17] This provides us with a variety of options to construct the shell with different properties, and to dissolve it if necessary. Furthermore, CaPs can easily form the complexes with biomolecules due to the occurrence of chelation between Ca^{2+} with biomolecule functional groups, ionic-covalent bonding with biomolecules, or electrostatic interaction between CaPs and biomolecules.[18,19] In other words, such a shell is easy to be further functionalized for theranostic applications. Due to these unique features, CaPs have been extensively utilized in nonviral gene delivery carriers for over 30 years and a number of CaP materials have been approved by US Food and Drug Administration (FDA) for biomedical applications in the last decade.[10,20–27] Recent advance in Ca^{2+} signaling and uptake has revealed the fateful encounter of mitochondria with calcium and CaPs,[28] thus mitochondria has gained a central role in regulation of cytoplasmic Ca^{2+} and storage of CaPs for cellular function.[28–30] As a result, CaP based carriers might be very beneficial and promising for intracellular delivery and mitochondria targeting compared with other carrying platforms which always require further functionalization to render them biocompatibility, intracellular delivery and subcellular targeting.

In this work, we chose ZnO QDs as the functional seeds for subcellular imaging due to the following factors. First, ZnO QDs offer excellent fluorescence properties compared with organic dyes including narrow emission peaks, broad absorption spectra, longer-fluorescence lifetime, photobleaching resistance, tunable emission colors by controlling the particle size, a broad of solvent types and surface modification.[31–34] Second, ZnO QDs are relatively biocompatible and considered biologically and environmentally safe compared with cadmium-based QDs. Thirdly, ZnO QDs have been found to have the potential in drug delivery related bio-imaging applications.[31,35–40] In general, the nanosized ZnO and CaPs turn out to be a good combination of high biocompatibility, biomolecule binding ability, and good fluorescence properties compared with other delivery systems. Nevertheless, an appropriate flesh is still needed in building up the optimized structure and sustaining the performance of ZnO QDs. The design and construction of ZnO/SiO_2@ACP nanostructures need to take into account the following facts: ZnO QDs as seeds are often synthesized in organic solvents to achieve the uniform distribution and to avoid the rapid fluorescence quenching, which normally occurs in aqueous phase. Therefore, the flesh selection and construction is crucial to control the appropriate size of ZnO seeds and protect them in aqueous solutions prior to ACP shell coating. In this regard, the amorphous silica flesh is selected to fulfill the following tasks: (a) to control the size of seeds, (b) to protect the ZnO seeds from quenching in aqueous solution, and (c) to facilitate the ACP shell formation. The seed-flesh-shell structure of the dragon fruits is given in **Figure 1**. The ZnO seeds are embedded inside the amorphous SiO_2 flesh, which is further covered by a thin shell of ACP.

Adv. Funct. Mater. **2016**,
DOI: 10.1002/adfm.201601481

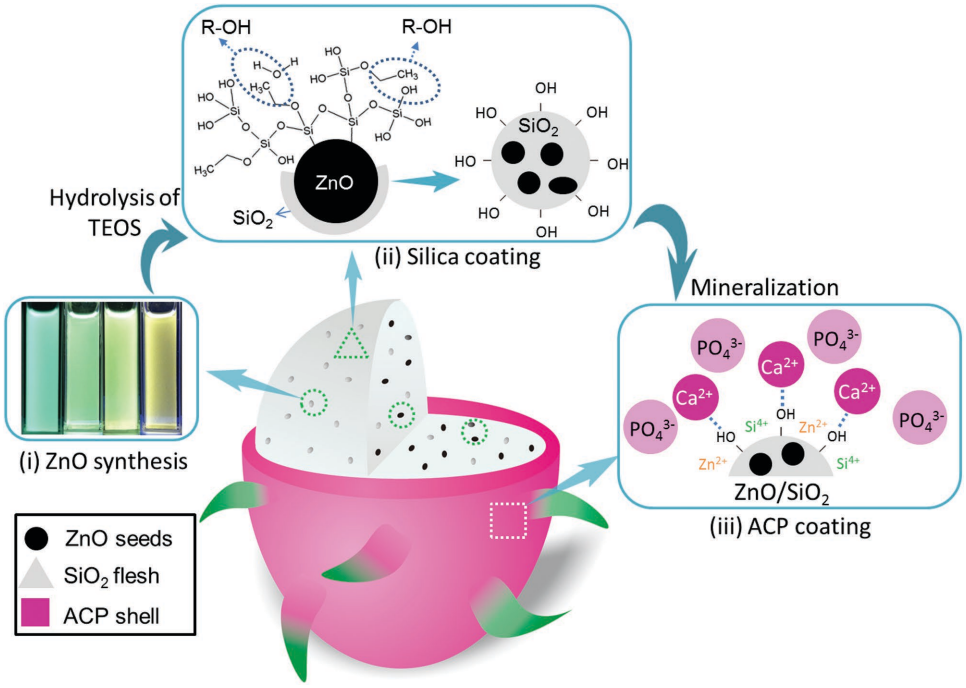

Figure 1. Schematic diagram showing the design of ZnO/SiO_2@ACP nanodragon fruits and the strategy of controlling fluorescent emission and delivered benefits. The dragon fruit provides a similar structure for the synthesized ZnO/SiO_2@ACP nano complex.

The strategy to engineer the fruit structure is illustrated in Figure 1. First of all, ZnO seeds are synthesized in organic solvents using a modified sol-gel method (Figure 1(i)).[41] Second, the freshly synthesized ZnO seeds are then embedded in the amorphous silica flesh. This is also a critical step in color selection which can be achieved by controlling the size via growing ZnO seeds in terms of tuning the supersaturation and the growth period of seeds (Figure 1(ii)). As the coating of amorphous silica will terminate the growth of ZnO seeds, the control of the application time of silica coating during the formation of ZnO seeds will acquire their desired size and the corresponding emission colors. In other words, the hydrolysis onset of silane precursor, TEOS on ZnO surface stops the growth and aggregation of seeds, giving rise to the color selection. Third, the seeded amorphous silica flesh will then be covered by the mineralization of ACP on the external surface (Figure 1(iii)). The ACP shell formation is based on the fact that there are the dangling silanol groups, known as Ca-binding sites and apatite promoters, on the silica surfaces.[42] ACP is subsequently mineralized by the accumulation of Ca^{2+} and PO_4^{3-} on the surface of ZnO/SiO_2 hybrids, which results in a high supersaturation of the precursor ions and the nucleation of ACP phases (Figure 1(iii)). In this paper, we demonstrate a simple approach to design and engineer a novel seed–flesh–shell, i.e., a dragon fruit structure of ZnO/SiO_2@ACP nanoparticles which allows their intracellular delivery and subcellular imaging of mitochondria. The effectiveness of ZnO/SiO_2@ACP nanofruits as intracellular nanoprobes was measured through the quantitative cellular uptake and subcellular distribution of the nanodragon fruits in mouse embryonic fibroblast NIH3T3 and human normal hepatic L02 cell lines.

2. Results and Discussions

2.1. Synthesis of ZnO Quantum Dots

The key step in the synthesis of ZnO QDs and the control of the fluorescent emission is determined by the control of ZnO QDs nucleation and growth. The nucleation and growth of ZnO QDs occurred right after mixing zinc acetate with sodium hydroxide in ethanol. **Figure 2** shows the typical emission spectra of ZnO QDs with time. The red shift of the emission peaks of the fluorescent spectra is due to the decrease of the band gap energy

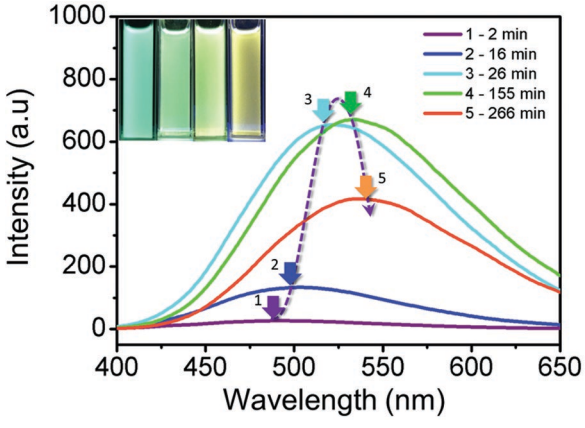

Figure 2. Fluorescence spectra of ZnO quantum dots versus time during the nucleation and growth. The growth of ZnO quantum dots is evidenced through the red shift in emission spectra. Inset shows the selection of emission colors by varying the supersaturation and coating with silica flesh.

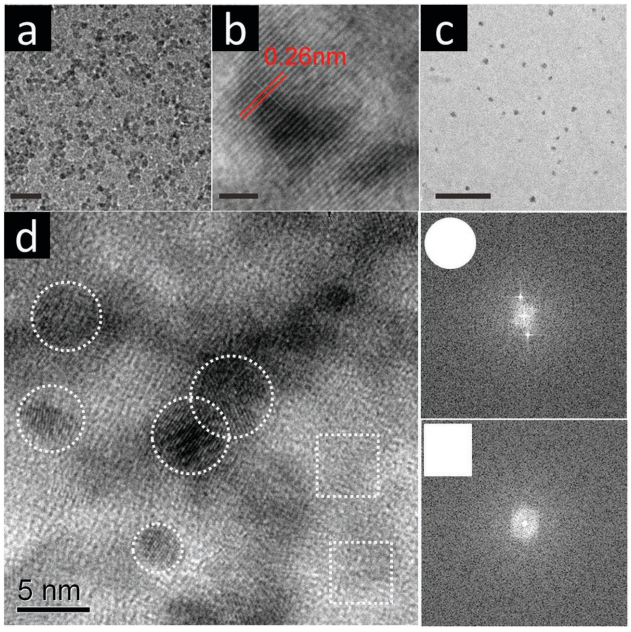

Figure 3. a) TEM images of ZnO quantum dots in ethanol (scale bar: 20 nm), b) HRTEM image of ZnO showing the (002) planes (scale bar 2 nm), c) monodisperse ZnO/SiO_2 nanoparticles in ethanol (scale bar: 200 nm), d) Left: ZnO crystal (circle) inside SiO_2 matrix (square), Right: FFT results showing crystalline phase of ZnO quantum dots (circle) and amorphous phase of silica matrix (square).

in addition to the reduction of quantum confinement energy, when the particle size increases.[43]

Transmission electron microscopy (TEM) data show the particle size of ZnO QDs around 5–7 nm (**Figure 3**a) and ZnO (002) crystal lattice planes (Figure 3b). The inset in Figure 2 shows the controlled colors of ZnO/SiO_2 from blue to green and to yellow emission.

2.2. Silica Flesh Formation

Figure 3c shows monodispersed ZnO/SiO_2 nanoparticles in ethanol. After the hydrolysis of tetraethyl orthosilicate (TEOS), ZnO QDs were securely kept within amorphous silica shells as shown by Figure 3d. The fast Fourier transform (FFT) patterns at selected regions (Figure 3d, right) show that crystalline ZnO QDs were embedded in amorphous SiO_2 matrix. The mechanism of silica shell formation was depicted in Figure 1(ii): Silica particles were formed by the hydrolysis of TEOS into $Si(OH)_4$ and subsequent condensation of $Si(OH)_4$ into SiO_2.[44]

2.3. ACP Shell Formation

The formation of ACP can be monitored by the pH of solutions. **Figure 4** shows the typical pH change as $CaCl_2$ was mixed with K_2HPO_4 at the initial pH ≈ 7. Amorphous calcium phosphate was rapidly formed after mixing and remained in solutions for a period of time, characterized by the duration of the first plateau. Posner's clusters were proposed as the approximate composition of ACP.[45] The first plateau attributed to the presence of ACP aggregates in the solutions. ACP nanoparticles were later transformed to hydroxyapatite (HAP, the most stable

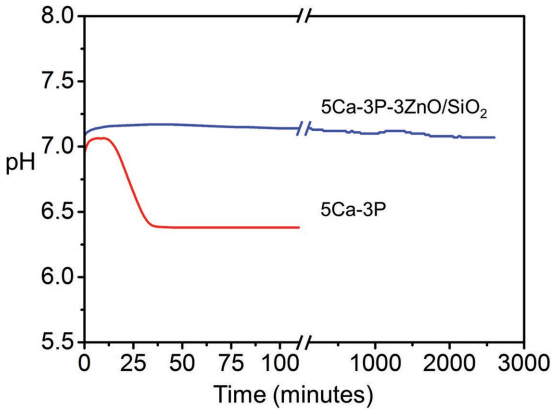

Figure 4. A plot of pH versus time during ACP formation with and without ZnO/SiO_2 nanoparticles showing the influence of ZnO/SiO_2 on ACP nucleation (5Ca-3P-3ZnO/SiO_2 means 5×10^{-3} M $CaCl_2 + 3 \times 10^{-3}$ M $K_2HPO_4 + 3 \times 10^{-3}$ M zinc acetate).

phase of CaPs with the formula $Ca_{10}(PO_4)_6(OH)_2$), giving rise to the rapid decrease of pH.[46–48] Once the reaction approaches the equilibrium, the pH reaches the minimum and keeps constant.

However, the pathway is altered completely once ZnO/SiO_2 nanoparticles are present. The value of pH kept almost unchanged and there is no dropdown of pH for a very long period of observation (Figure 4). This means that no conversion from ACP to HAP occurs, implying that ACP shells were stabilized by ZnO/SiO_2 nanoparticles. The stability of ACP on ZnO/SiO_2 particles in our study is unusual as silica is known to promote HAP formation.[42,49] This unusual ACP stability might be originated from the complex surface structure of ZnO/SiO_2 (as shown in Figure 1(iii)) which is rich in Zn^{2+} also known as an inhibiting agent for HAP formation.[50,51]

The Fourier transform infrared (FTIR) and X-ray diffraction (XRD) spectra of the as-prepared ZnO/SiO_2 and ZnO/SiO_2@ACP powders also further confirm the presence of ACP on hybrid ZnO/SiO_2 nanoparticles (**Figure 5**). The FTIR spectrum shows two featureless bands at 550 and 997 cm^{-1} which characterize the occurrence of ACP (Figure 5a).[52] XRD spectra show no visible peaks of ACP phases in ZnO/SiO_2@ACP samples (Figure 5b). For ZnO/SiO_2 samples, FTIR spectrum shows Si–O stretching band at 978 cm^{-1}, and XRD results show visible peaks (marked with an asterisk) of hexagonal crystalline structure of ZnO QDs.

The nanosized dragon fruit structure is clearly demonstrated in **Figure 6**a showing ZnO seeds embedded in silica flesh, which are further encapsulated in the ACP shells. For comparison, the inset in Figure 6a shows a real dragon fruit to illustrate the seed–flesh–shell structure. Figure 6 b and c show a cluster of nanosized dragon fruits and the corresponding selected area electron diffraction (SAED) respectively, which confirms the amorphous phase of ZnO/SiO_2 @ACP. The elemental analysis using energy dispersive X-ray spectroscopy (EDS) (Figure 6d) confirms the presence of Ca, P, Zn, Si, O elements with the ratio of Ca/P = 1.16.

The stabilization effect of silica and ACP coating on the fluorescent emission spectra is demonstrated in **Figure 7**. In comparison, the neat ZnO seeds show the red shift of the

Adv. Funct. Mater. **2016**,
DOI: 10.1002/adfm.201601481

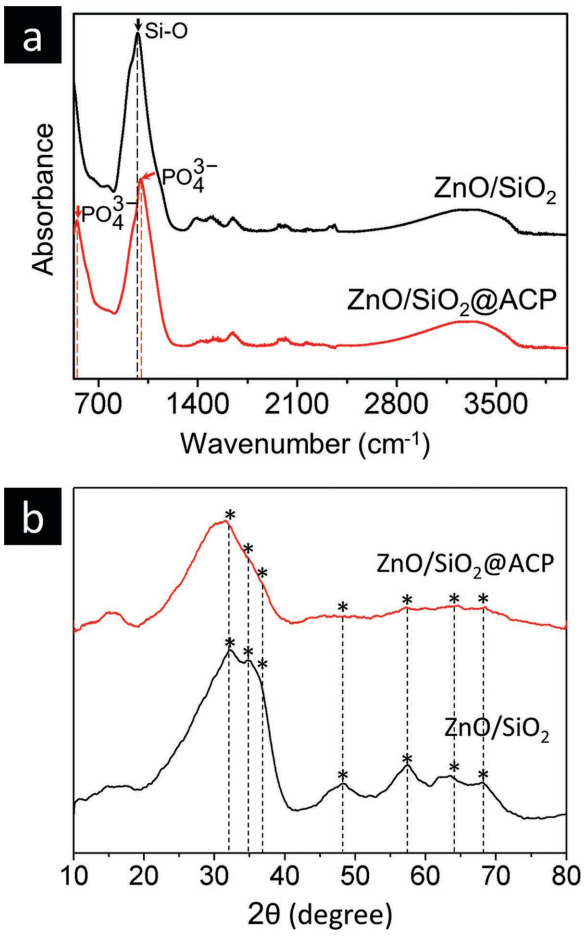

Figure 5. a) FTIR and b) XRD spectra of hybrid ZnO/SiO_2 and core–shell ZnO/SiO_2@ACP nanostructures.

emission spectra and the significant reduction of the fluorescent intensity over 10 h storage in ethanol solvent. This indicates strongly the serious aggregation and quenching of ZnO seeds over time. In contrast, the hybrid ZnO/SiO_2 core-shell and the ZnO/SiO_2@ACP nanosized dragon fruits only show a mild reduction of the fluorescent intensity for more than four months storage in aqueous solutions and the fluorescent peaks remain the same. This implies no aggregation of ZnO seeds after coating with silica and ACP. In other words, silica coating improves the fluorescent emission stability of ZnO seeds over time and ACP coating does not jeopardize that of hybrid ZnO/SiO_2 nanoparticles. It is worth noting that the fruit structure and the emission colors remain for a long period of time either in aqueous solutions or in the dry state (solid form) (Figure S1, Supporting Information and Figure 7). The mild reduction of the fluorescent intensity of hybrid ZnO/SiO_2 core–shell and ZnO/SiO_2@ACP nanosfruits over time is probably due to the following facts: (i) the aggregation of ZnO/SiO_2@ACP nanosized dragon fruits and the precipitate occurred (Figure S2, Supporting Information) (ii) the diffusion of water molecules into the silica flesh and their subsequent reaction with the emission centers of ZnO seeds to form Zn^{2+} ions, which diffuse down the concentration gradient out of the silica fleshes and shells. In any case, the direct aggregation and the quenching of ZnO seeds do not occur. In other words, they are well protected by the seed–flesh–shell structure of dragon fruits.

2.4. Intracellular Delivery and Subcellular Imaging of Mitochondria

The effectiveness of ZnO/SiO_2@ACP nanofruits as intracellular nanoprobes was measured through the quantitative cellular uptake and subcellular distribution. In this regard, the NIH3T3 and L02 cell lines were adopted to investigate the cellular uptake profile of the nanofruits. We compared the cytotoxicity of ZnO/SiO_2@ACP with ZnO/SiO_2 and found that ZnO/SiO_2@ACP showed little cytotoxicity at and below 50 μg mL^{-1}, while that of ZnO/SiO_2 was at and below 10 μg mL^{-1} in NIH3T3 cells (**Figure 8**). This result suggests that ZnO/SiO_2@ACP nanofruits are more biocompatible than ZnO/SiO_2 nanoparticles and ACP shells do serve as the designated task.

The cellular uptake of nanofruits was assessed using confocal laser scanning microscopy (CLSM) and quantitative real-time PCR (qRT-PCR). **Figure 9** shows that the green fluorescence of ZnO/SiO_2@ACP nanofruits emitted from the cytoplasma and the fluorescence intensity increased with incubation time.

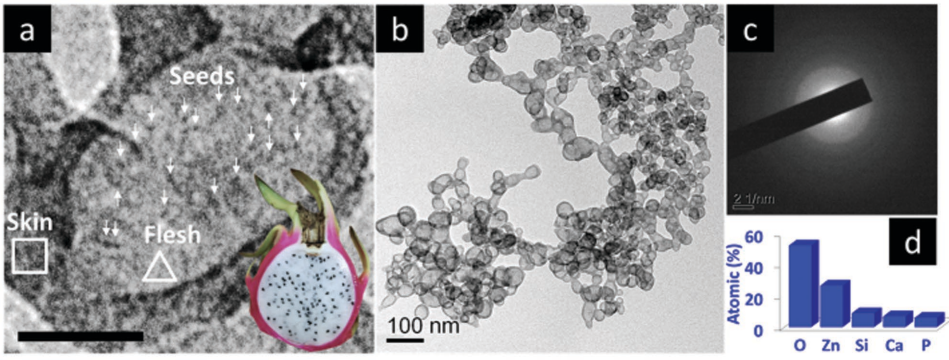

Figure 6. a) TEM image of a single ZnO/SiO_2@ACP nanostructures (scale bar: 20 nm) including ZnO seeds, silica flesh, and ACP shell that are marked with arrows, triangle and square, respectively. Inset is a cross-section photo of a dragon fruit for structural comparison. b) TEM image of ZnO-SiO_2-ACP cluster, c) selected area electron diffraction, and d) EDS analysis of ZnO/SiO_2@ACP nanostructures.

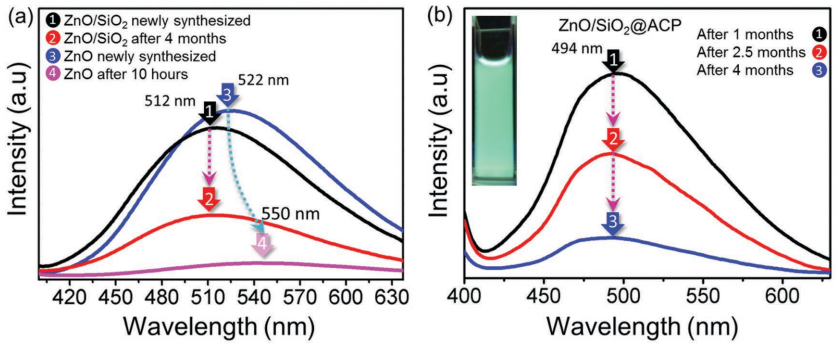

Figure 7. Time course of fluorescent spectra of a) ZnO QDs, hybrid ZnO/SiO_2 (excited at 330 nm) and b) ZnO/SiO_2@ACP nanofruits (excited at 338 nm).

Confocal microscopy analysis of nanofruit-treated cells labeled with Lysotracker and Mitotracker shows that nanofruits were located at lysosome and mitochondria in both cell lines (**Figures 10** and **11**). This confirms that ZnO/SiO_2@ACP nanofruits are able to target the mitochondria; therefore this new nanofruit platform can be a promising candidate for subcellular imaging and intracellular delivery of active agents to mitochondria for related diseases.

The above results demonstrate that the dragon fruit-like ZnO/SiO_2@ACP nanostructures do produce the designated effect over the conventional nanocarriers: (i) all ingredients are considered safe in the biomimetic structure (Zn, Si, Ca, P are all essential elements for living organisms); (ii) the color emission can be selected at will from blue to yellow, and acquired a better control over organic dyes or other fluorophores; (iii) the ZnO seeds are protected from fluorescent quenching and aggregation in aqueous solutions by the silica flesh and ACP shell; (iv) the nanodragon fruits of ZnO/SiO_2@ACP are more biocompatible owing to the formation of the silica flesh and ACP shell, which are "generally recognized as safe" (GRAS) by the US FDA; (v) the coating of ACP on ZnO/SiO_2 does elevate the biocompatibility of ZnO/SiO_2@ACP nanofruits; (vi) the prepared nanosized dragon fruit is suitable for intracellular delivery

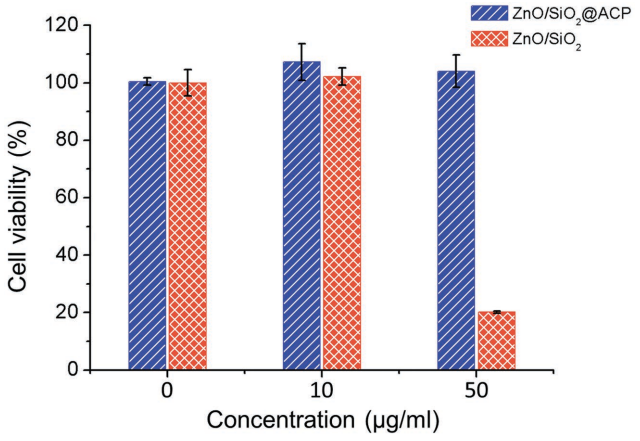

Figure 8. Cell viability of NIH3T3 treated with ZnO/SiO_2@ACP and ZnO/SiO_2 for 24 h as measured using MTS assay. This result shows that ZnO/SiO_2@ACP is more biocompatible than ZnO/SiO_2.

targeting mitochondria which play significant roles in numerous human disorders related to mitochondrial dysfuntions, e.g., inflammation, neurodegeneration, obesity, diabetes, cardiovascular diseases, cancer, aging related diseases, etc.[6] In addition, the pH-dependent solubility of ACP equips the ZnO/SiO_2@ACP nanofruits with the controlled release manner; the high dissolution rate of ACP at low pH media facilitates the delivery of drugs into the malign zones. The ZnO/SiO_2@ACP nanofruits with ACP shell also provide the high binding affinity with DNA, proteins or other biomolecules, thus can be potentially applied in gene therapy, e.g., gene transfection or gene silencing, targeted delivery.

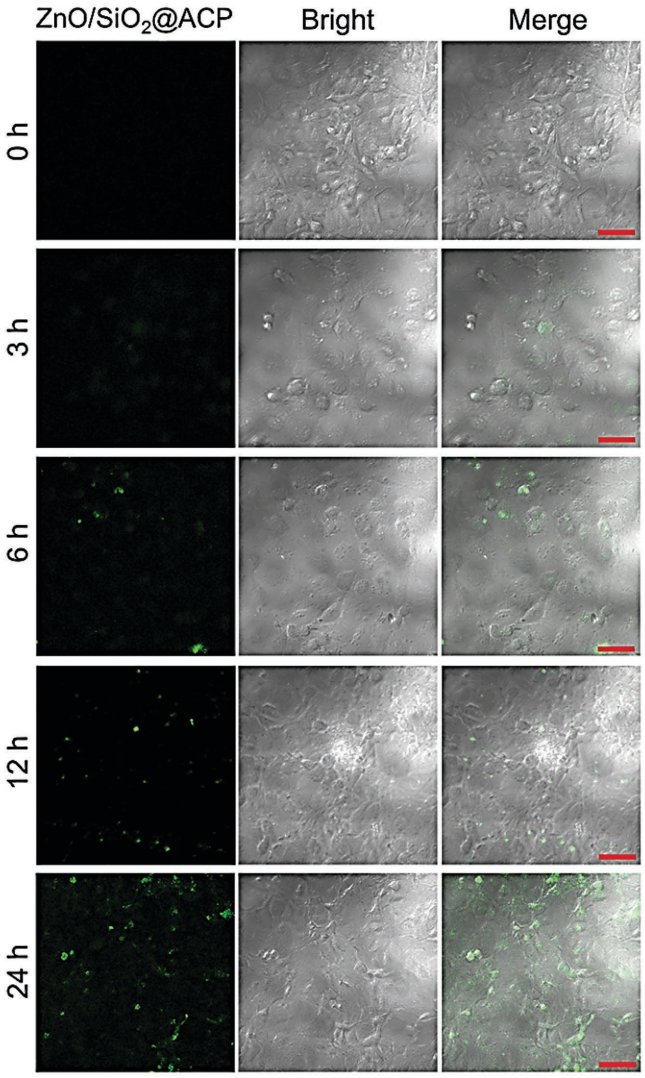

Figure 9. The ZnO/SiO_2@ACP nanosfruits were internalized by cells and observed using confocal laser scanning microscopy. The green fluorescence of ZnO/SiO_2@ACP nanofruits emitted from the cytoplasma and the fluorescence intensity increased from 0 to 24 h. Scale bar is 50 μm.

Adv. Funct. Mater. **2016**,
DOI: 10.1002/adfm.201601481

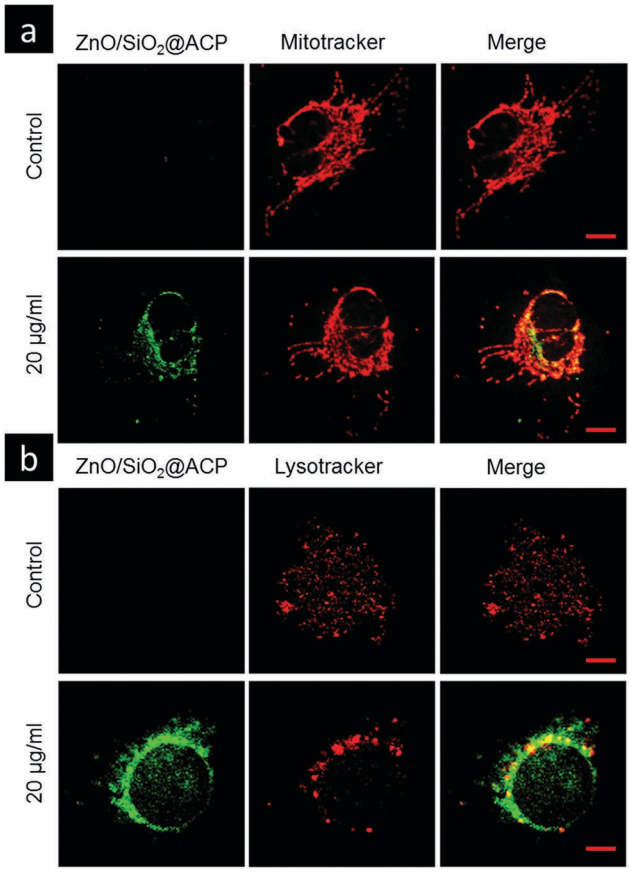

Figure 10. ZnO/SiO_2@ACP nanofruit colocation with a) mitochondria and b) lysosome in NIH3T3 cells. Cells were treated with 20 μg mL^{-1} nanofruits for 12 h, then they were incubated with Mitotracker or Lysotracker for 30 min and observed using CLSM. Scale bar is 5 μm.

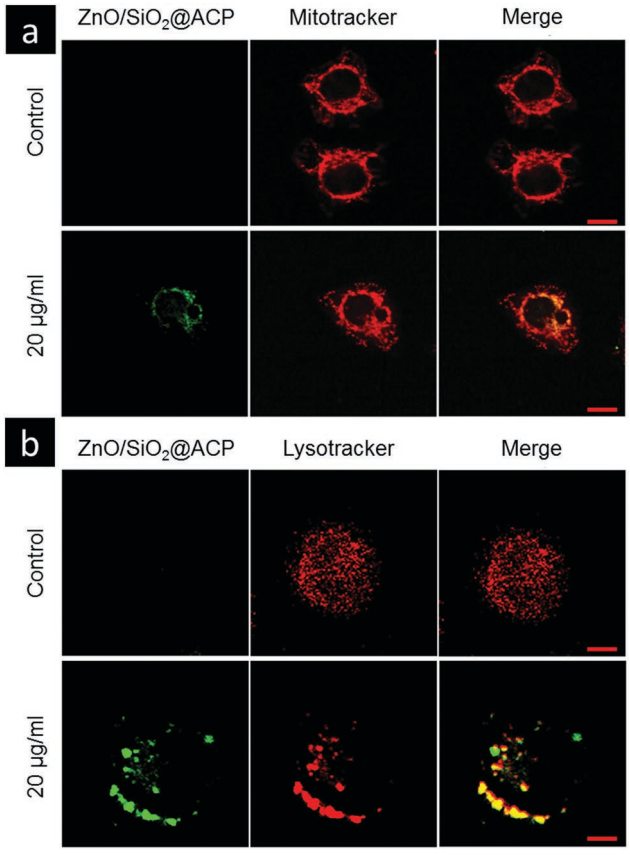

Figure 11. ZnO/SiO_2@ACP nanofruit colocation with a) mitochondria and b) lysosome in in L02 cells. Cells were treated with 20 μg mL^{-1} nanofruits for 12 h, then they were incubated with Mitotracker or Lysotracker for 30 min and observed using CLSM. Scale bar is 5 μm.

Moreover, the silica flesh can be loaded with drugs, functional moieties, or extra sensing agents, e.g., magnetic cores.[53,54] These advantageous effects make ZnO/SiO_2@ACP nanofruits a promising candidate in bioimaging, drug delivery, cancer treatment, and gene therapy with multifunctional, controlled release, and smart responsive manners.[10,55]

Furthermore, the seed–flesh–shell structure provides extra functionalities that can be utilized for various applications, such as the protection of sensing and active agents (functional seeds), the separation of incompatible ingredients (e.g., one in the flesh, the other in the shell) for a broader range of drug and sensing agent selection, and the multifunctionalization of both the flesh and the shell for the controlled release and targeted delivery. The structure also provides more parameters, e.g., constituents, composition, the core to shell thickness ratio in controlling performance outcome.[56] As one of the outcomes, one can expect that the seed–flesh–shell structure would offer the high loading capacity, superior reactivity, a variety of binding possibilities, multifunctions, and controlled electrical, optical, or magnetic properties, controlled and sustained release, targeted delivery, diagnostic, bioimaging, and biosensing.[56–59]

3. Conclusions

In this study, we demonstrate that a rational design of nanofruits can deliver favorable outcomes: elevated biocompatibility, intracellular delivery efficiency, subcellular targeting, and controlled release manner. The nanofruits also offer substantial enhancement in fluorescent stability of the functional seeds in aqueous solution or in the dry state, precise color selection, and the stability of short-lived ACP which is highly biocompatible and bioresorbable. More interestingly, this new nanodragon fruit ZnO/SiO_2@ACP can be used in targeting and imaging of mitochondria, which aid treatment and diagnostic of related diseases. The strategy of "biomimicking" the ZnO/SiO_2@ACP nanodragon fruit structure relies mainly on the knowledge of the formation of the individual components (the seed, the flesh, and the shell) and the factors controlling their nucleation, e.g., supersaturation, pH, solvents, additives. This can be further extended to other hybrid nanomaterial systems provided that prior knowledge on the formation of the seeds, the flesh, and the shell, and all controlling factors should be well conceived.

4. Experimental Section

Preparation of ZnO/SiO_2@ACP Nanofruits: All reagents were used as received without further purification. All reactions were conducted at room temperature ≈23 °C and under vigorous stirring by Teflon-coated magnetic stirrer. ZnO QDs were synthesized using a modified sol-gel method.[41] Zinc acetate and sodium hydroxide were both dissolved in ethanol with the concentration 100×10^{-3} M, and 1 M, respectively. Then zinc acetate solution was mixed with sodium hydroxide solution with the varied ratio of zinc acetate:sodium hydroxide to control the emission colors. The emission colors of ZnO QDs in the inset of Figure 2 were obtained by using a wide range of zinc acetate:sodium hydroxide ratios, e.g., 20:50, 20:20, 10:40, etc. (mM). The mixtures were placed under a fluorescent spectrometer right after mixing to study the dynamic formation of ZnO QDs by recording the emission spectra of the reacting solutions with time. TEOS and water was added into the mixtures with the ratio of zinc acetate:TEOS:H_2O = 1:1:2 (molarity) at the interval of 10, 15, 20, 25, 30, 40 min, etc. after the onset of acetate-sodium hydroxide mixing based upon the time evolution curves of the emission spectra of ZnO QDs. The solutions were left overnight and then collected by centrifuge and washed two times with ethanol, one time with deionized (DI) water. The precipitation was later transferred into an equal amount of aqueous solution with final pH fixed at 7 for mineralization of ACP. The precursors of ACP were $CaCl_2$ 1 M and K_2HPO_4 1 M in DI water. $CaCl_2$ and K_2HPO_4 were mixed with the aqueous ZnO-SiO_2 solution at final concentration 10:6 (mM). The reaction of the mixture was monitored by pH meter. The final products were either stored for months in solution or in dry state by centrifugation followed by washing with DI water two times then drying in the oven at 60 °C. The dried powder was later used for XRD and FTIR analysis.

Characterization of ZnO/SiO_2@ACP Nanostructures: Fluorescent spectra measurements were conducted using Varian Cary Eclipse Fluorescence Spectrophotometer at room temperature. Immediately after mixing zinc acetate and NaOH, 3–4 mL of reacting solutions were put in a quartz cuvette. The cuvette was then sealed into the closed fluorescence chamber for measurement.

Morphology of ZnO/SiO_2@ACP nanofruits were studied using scanning electron microscopy (JEM 6700F, JEOL, Japan). Transmission electron microscopy (JEM 3010F, JEOL, Japan) was used to study the core–shell structure, phase and elemental analysis of ZnO/SiO_2@ACP nanofruits. XRD analysis of ZnO/SiO_2@ACP nanofruits was also conducted.

Cell Culture and Viability: NIH3T3 and L02 cells were maintained in RPMI-1640 medium supplemented with 10% fetal bovine serum (FBS) and 1% penicillin & streptomycin (Gibco, NY, USA) at 37 °C in a 5% CO_2 humidified incubator (Thermo, CO, USA). MTS assay was conducted to measure cell viability (Promega, USA). NIH3T3 cells were seeded on 96-well plates (10 000 per well) overnight, then incubated with 0, 10, 20, 40, 60, and 80 μg mL^{-1} of ZnO/SiO_2@ACP nanostructures for 12 and 24 h. Before absorbance measurement 3 h, the MTS reagent was added. The absorbance at 490 nm was assessed with the microplate spectrophotometer (Mutiscan, Thermo, USA).

Cellular Fluorescence Imaging Using Confocal Microscopy: To investigate the cell uptake and imaging of ZnO/SiO_2@ACP nanostructures, cells were seeded on coverslips overnight, and then incubated with 20 μg mL^{-1} of nanofruits (a negotiable cytotoxic concentration) for 12 h. The nanofruit-treated cells were reacted with MitoTracker Orange probe or LysoTracker Red probe (Invitrogen, CA, USA) for 30 min at humidified incubator according to the manufacturer's manual. The treated cells were fixed with 4% paraformaldehyde for 15 min and washed twice in PBS, then visualized using a CLSM (Olympus, Tokyo, Japan). The wavelengths of excitation of MitoTracker Orange, LysoTracker Red, and nanofruits were 579, 570, and 324 nm respectively, and those of emission were 599, 590, and 512 nm, respectively.

Quantitative Real-Time PCR (qRT-PCR): Total RNA was extracted from cells using Trizol (Life, USA). 1st chain cDNA synthesis was conducted according to the manufacturer's instruction (Takara, Dalian, China). The primers were as follow: *MT1B* forward primer, 5′-GGC TTG TCT TGG CTC CAA ATG-3′; *MT1B* reverse primer, 5′-GCA AAC CGG TCA GGG TAG TT-3′; *MT2A* forward primer 5′-GCA ACC TGT CCC GAC TCT AG-3′; *MT2A* reverse primer, 5′-GGT CAC GGT CAG GGT TGT AC-3′; *ACTB* forward primer, 5′-CAC CAG GGC GTG ATG GT-3′; *ACTB* reverse primer, 5′-CTC AAA CAT GAT CTG GGT CAT-3′. The qRT-PCR was conducted using a BioRad CFX96 Real Time PCR system (BioRad, USA). Each reaction contained 1 μL of 1st chain cDNA as template with 0.3 pmol of each primer, 5 μL SYBR Green PCR Master Mix, and up to 10 μL with double distilled H_2O. The reaction condition was initial denaturation at 94 °C for 3 min, followed by 40 cycles of 94 °C for 10 s, and 60 °C for 34 s. mRNA relative expression levels were fold of *ACTB* according to the formula $2^{\triangle Ct \text{ (untreated target gene- untreated } ACTB) - \triangle Ct \text{(treated target gene- treated } ACTB)}$. The assays were performed in duplicate and repeated with three independent experiments.

Supporting Information

Supporting Information is available from the Wiley Online Library or from the author.

Acknowledgements

This work was supported by Singapore AcRF Tier 1 (R-144-000-348-112), China government funding (Nos. 21404087, U1405226, 0620-K32006, and 2014H6022, NSFC Nos. 81402648 and 81472997), "111" Project (B16029), the 1000 Talents Program from Xiamen University; Early-stage Project of National Key Basic Research Program of China (No. 2014CB560710) and Scientific and Technological Innovation Platform of Fujian Province (2014H2006).

Received: March 23, 2016
Revised: May 27, 2016
Published online:

[1] J. Hemminger, G. Crabtree, J. Sarrao, *Tech. Rep* **2012**, 1601.
[2] N. Lin, X.-Y. Liu, *Chem. Soc. Rev.* **2015**, *44*, 7881.
[3] *Bioinspiration From Nano to Micro Scales* (Ed: X. Y. Liu), **2012**, p. , Springer, New York.
[4] S. Weiner, H. D. Wagner, *Annu. Rev. Mater. Sci.* **1998**, *28*, 271.
[5] L. Addadi, D. Joester, F. Nudelman, S. Weiner, *Chem. Eur. J.* **2006**, *12*, 980.
[6] S. Marrache, S. Dhar, *Proc. Natl. Acad. Sci. USA* **2012**, *109*, 16288.
[7] A. M. Derfus, W. C. W. Chan, S. N. Bhatia, *Nano Lett* **2004**, *4*, 11.
[8] C. Kirchner, T. Liedl, S. Kudera, T. Pellegrino, A. M. Javier, H. E. Gaub, S. Stolzle, N. Fertig, W. J. Parak, *Nano Lett.* **2005**, *5*, 331.
[9] A. H. Faraji, P. Wipf, *Bioorg. Med. Chem.* **2009**, *17*, 2950.
[10] M. Epple, K. Ganesan, R. Heumann, J. Klesing, A. Kovtun, S. Neumann, V. Sokolova, *J. Mater. Chem.* **2010**, *20*, 18.
[11] S. V. Dorozhkin, M. Epple, *Angew. Chem. Int. Ed.* **2002**, *41*, 3130.
[12] D. Aronov, A. Karlov, G. Rosenman, *J. Eur. Ceram. Soc.* **2007**, *27*, 4181.
[13] S. B. Lang, S. A. M. Tofail, A. A. Gandhi, M. Gregor, C. Wolf-Brandstetter, J. Kost, S. Bauer, A. M. Krause, *Appl. Phys. Lett.* **2011**, *98*, 123703.
[14] G. H. Nancollas, B. Tomazic, *J. Phys. Chem.* **1974**, *78*, 2218.
[15] Y. Wang, M. S. Hassan, P. Gunawan, R. Lau, X. Wang, R. Xu, *J. Colloid Interface Sci.* **2009**, *339*, 69.
[16] K. Yamashita, N. Oikawa, A. T. Umegaki, *Chem. Mater.* **1996**, *8*, 2697.
[17] P. Zhu, Y. Masuda, K. Koumoto, *Biomaterials* **2004**, *25*, 3915.

[18] M. J. Gorbunoff, S. N. Timasheff, *Anal Biochem.* **1984**, *136*, 440.
[19] M. J. Gorbunoff, *Methods Enzymol.* **1985**, *117*, 370.
[20] F. L. Graham, A. J. van der Eb, *Virology* **1973**, *52*, 456.
[21] Q. He, A. R. Mitchell, S. L. Johnson, C. Wagner-Bartak, T. Morcol, S. J. D. Bell, *Clin. Diagn. Lab Immunol.* **2000**, *7*, 899.
[22] D. Olton, J. Li, M. E. Wilson, T. Rogers, J. Close, L. Huang, P. N. Kumta, C. Sfeir, *Biomaterials* **2007**, *28*, 1267.
[23] T. T. Morgan, H. S. Muddana, E. I. Altinoglu, S. M. Rouse, A. Tabakovic, T. Tabouillot, T. J. Russin, S. S. Shanmugavelandy, P. J. Butler, P. C. Eklund, J. K. Yun, M. Kester, J. H. Adair, *Nano Lett.* **2008**, *8*, 4108.
[24] M. Kester, Y. Heakal, T. Fox, A. Sharma, G. P. Robertson, T. T. Morgan, E. I. Altinoglu, A. Tabakovic, M. R. Parette, S. M. Rouse, V. Ruiz-Velasco, J. H. Adair, *Nano Lett.* **2008**, *8*, 4116.
[25] B. M. Barth, R. Sharma, E. İ. Altınoğlu, T. T. Morgan, S. S. Shanmugavelandy, J. M. Kaiser, C. McGovern, G. L. Matters, J. P. Smith, M. Kester, J. H. Adair, *ACS Nano* **2010**, *4*, 1279.
[26] J. Li, Y.-C. Chen, Y.-C. Tseng, S. Mozumdar, L. Huang, *J Controlled Release* **2010**, *142*, 416.
[27] J. Li, Y. Yang, L. Huang, *J. Controlled Release* **2012**, *158*, 108.
[28] E. Carafoli, *Biochim. Biophys. Acta* **2010**, *1797*, 595.
[29] A. L. Lehninger, *Biochem. J.* **1970**, *119*, 129.
[30] D. G. Nicholis, S. Chalmers, *J. Bioenerg. Biomembr.* **2004**, *36*, 277.
[31] X. Tang, E. S. G. Choo, L. Li, J. Ding, J. Xue, *Chem. Mater.* **2010**, *22*, 3383.
[32] Z. Hu, G. Oskam, P. C. Searson, *J. Colloid Interface Sci.* **2003**, *263*, 454.
[33] R.-O. Moussodia, L. Balan, C. Merlin, C. Mustind, A. R. Schneider, *J. Mater. Chem.* **2010**, *20*, 1147.
[34] H. M. Xiong, Y. Xu, Q. G. Ren, Y. Y. Xia, *J. Am. Chem. Soc.* **2008**, *130*, 7522.
[35] X. Tang, E. S. G. Choo, L. Li, J. Ding, J. Xue, *Langmuir* **2009**, *25*, 5271.
[36] H.-M. Xiong, Y. Xu, Q.-G. Ren, Y.-Y. Xia, *J. Am. Chem. Soc.* **2008**, *130*, 7522.
[37] Q. Yuan, S. Hein, R. D. K. Misra, *Acta Biomater.* **2010**, *6*, 2732.
[38] R.-O. Moussodia, L. Balan, C. Merlin, C. Mustind, R. Schneider, *J. Mater. Chem.* **2010**, *20*, 1147.
[39] M. Sato, H. Harada, S. Morito, Y. Fujita, S. Shimosaki, T. Urano, M. Nakamura, *Appl. Surf. Sci.* **2010**, *256*, 4497.
[40] H.-M. Xiong, *Adv. Mater.* **2013**, *25*, 5329.
[41] L. Spanhel, M. A. Anderson, *J. Am. Chem. Soc.* **1991**, *113*, 2826.
[42] P. J. Li, C. Ohtsuki, T. Kokubo, K. Nakanishi, N. Soga, T. Nakamura, T. Yamamuro, *J. Am. Ceram. Soc.* **1992**, *75*, 2094.
[43] L. E. Brus, *J. Chem. Phys.* **1984**, *80*, 4403.
[44] W. Stöber, A. Fink, *J. Colloid Interface Sci.* **1968**, *26*, 62.
[45] A. S. Posner, F. Betts, *Acc. Chem. Res.* **1975**, *8*, 273.
[46] H. H. Pan, X. Y. Liu, R. K. Tang, H. Y. Xu, *Chem. Commun.* **2010**, *46*, 7415.
[47] F. Betts, N. C. Blumenthal, A. S. Posner, G. L. Becker, A. L. Lehninger, *Proc. Natl. Acad. Sci. USA* **1975**, *72*, 2088.
[48] H. Furedi-Milhofer, L. Brecevic, B. Purgaric, *Faraday Discuss. Chem. Soc.* **1976**, *61*, 184.
[49] S.-B. Cho, K. Nakanishi, T. Kokubo, N. Soga, C. Ohtsuki, T. Nakamura, *J. Biomed. Mater. Res.* **1996**, *33*, 145.
[50] T. A. Fuierer, M. LoRe, S. A. Puckett, G. H. Nancollas, *Langmuir* **1994**, *10*, 4721.
[51] N. Kanzaki, K. Onuma, G. Treboux, S. Tsutsumi, A. Ito, *J. Phys. Chem. B* **2000**, *104*, 4189.
[52] S. Somrani, C. Rey, M. Jemalc, *J. Mater. Chem.* **2003**, *13*, 888.
[53] J. M. Rosenholm, C. Sahlgren, M. Linden, *Curr. Drug Targets* **2011**, *12*, 1166.
[54] M. Liong, J. Lu, M. Kovochich, T. Xia, S. G. Ruehm, A. E. Nel, F. Tamanoi, J. I. Zink, *ACS Nano* **2008**, *2*, 889.
[55] V. Uskokovic, D. P. Uskokovic, *J. Biomed. Mater. Res. B* **2011**, *96B*, 152.
[56] R. G. Chaudhuri, S. Paria, *Chem. Rev.* **2012**, *112*, 2373.
[57] D. Kashchiev, *Nucleation Basic Theory with Applications*, Butterworth-Heinemann, Oxford **2000**.
[58] M. A. Meyers, A. Mishra, D. J. Benson, *Prog. Mater. Sci.* **2006**, *51*, 427.
[59] M. Grätzel, *Nature* **2001**, *414*, 338.